Journal of Geophysical Research: Oceans

RESEARCH ARTICLE

10.1002/2017JC012845

Key Points:

- Recent decadal changes in subpolar North Atlantic heat content are due to advective heat flux convergences by midlatitude ocean transports
- Horizontal gyre circulations contribute more to advective convergences than vertical overturning circulations at 46°N
- Anomalous gyre circulation strongly covaries with local wind stress curl, suggesting a role for Sverdrup dynamics

Supporting Information:

- Supporting Information S1

Correspondence to:
C. G. Piecuch,
cpiecuch@aer.com

Citation:
Piecuch, C. G., R. M. Ponte, C. M. Little, M. W. Buckley, and I. Fukumori (2017), Mechanisms underlying recent decadal changes in subpolar North Atlantic Ocean heat content, *J. Geophys. Res. Oceans*, *122*, 7181–7197, doi:10.1002/2017JC012845.

Received 28 FEB 2017
Accepted 17 AUG 2017
Accepted article online 25 AUG 2017
Published online 8 SEP 2017

Mechanisms underlying recent decadal changes in subpolar North Atlantic Ocean heat content

Christopher G. Piecuch[1], **Rui M. Ponte**[1], **Christopher M. Little**[1], **Martha W. Buckley**[2], and **Ichiro Fukumori**[3]

[1]Atmospheric and Environmental Research, Inc., Lexington, Massachusetts, USA, [2]Atmospheric, Oceanic, and Earth Sciences, George Mason University, Fairfax, Virginia, USA, [3]Jet Propulsion Laboratory, California Institute of Technology, Pasadena, California, USA

Abstract The subpolar North Atlantic (SPNA) is subject to strong decadal variability, with implications for surface climate and its predictability. In 2004–2005, SPNA decadal upper ocean and sea-surface temperature trends reversed from warming during 1994–2004 to cooling over 2005–2015. This recent decadal trend reversal in SPNA ocean heat content (OHC) is studied using a physically consistent, observationally constrained global ocean state estimate covering 1992–2015. The estimate's physical consistency facilitates quantitative causal attribution of ocean variations. Closed heat budget diagnostics reveal that the SPNA OHC trend reversal is the result of heat advection by midlatitude ocean circulation. Kinematic decompositions reveal that changes in the deep and intermediate vertical overturning circulation cannot account for the trend reversal, but rather ocean heat transports by horizontal gyre circulations render the primary contributions. The shift in horizontal gyre advection reflects anomalous circulation acting on the mean temperature gradients. Maximum covariance analysis (MCA) reveals strong covariation between the anomalous horizontal gyre circulation and variations in the local wind stress curl, suggestive of a Sverdrup response. Results have implications for decadal predictability.

1. Introduction

The subpolar North Atlantic (SPNA) shows strong sea-surface temperature (SST) and ocean heat content (OHC) variability over decadal and multidecadal periods [e.g., *Lozier et al.*, 2008, 2010; *Häkkinen et al.*, 2011a,2011b,2013; *Robson et al.*, 2014, 2016; *Williams et al.*, 2014, 2015; *McCarthy et al.*, 2015; *Menary et al.*, 2015; *Buckley and Marshall*, 2016]. These thermal variations have a strong impact on surface climate over the Atlantic sector. For example, a dominant mode of Atlantic SST variability—the Atlantic multidecadal variability (AMV)—is most apparent over the SPNA [*Schlesinger and Ramankutty*, 1994]. The AMV has been related to changes in Atlantic hurricane activity and tropospheric vertical shear, anomalous North American and European river flow and rainfall, and shifts in the Intertropical Convergence Zone and rainfall over northeastern Brazil and the African Sahel [*Sutton and Hodson*, 2005; *Knight et al.*, 2006; *Zhang and Delworth*, 2006]. Decadal SPNA SST and OHC variations also show correlation with cryospheric changes, including Greenland ice sheet discharge, rates of Northern Hemisphere sea-ice loss, and mass balance of glaciers in the Swiss Alps [*Huss et al.*, 2010; *Straneo and Heimbach*, 2013; *Zampieri et al.*, 2013; *Yeager et al.*, 2015; *Frajka-Williams et al.*, 2016]. Understanding SPNA SST and OHC changes and their predictability on decadal and longer time scales has thus been a major goal in climate research [*Keenlyside et al.*, 2008; *Dunstone et al.* 2011; *Yeager et al.*, 2012; *Roberts et al.*, 2016].

Despite its importance in climate, the mechanisms underlying decadal and multidecadal SPNA changes remain incompletely understood. Various mechanisms have been proposed (sinking of water masses, interaction with the western boundary, propagation of planetary waves, etc.), whose relevance could depend on the specific periods, regions, frequencies, and wave numbers under consideration [*Menary et al.*, 2015; *Buckley and Marshall*, 2016]. Over the last two decades, the SPNA has undergone a pronounced climate shift. Decadal OHC and SST trends reversed sign around 2004–2005, with a strong warming seen during 1994–2004 and marked cooling observed over 2005–2015. These trend reversals were pronounced ($>$0.1°C yr^{-1} in magnitude) in the northeastern North Atlantic (south and west of Iceland) and in the Labrador Sea (Figure 1). Based on reanalysis fields, *Robson et al.* [2016] (hereafter R16) argue that this decadal climate

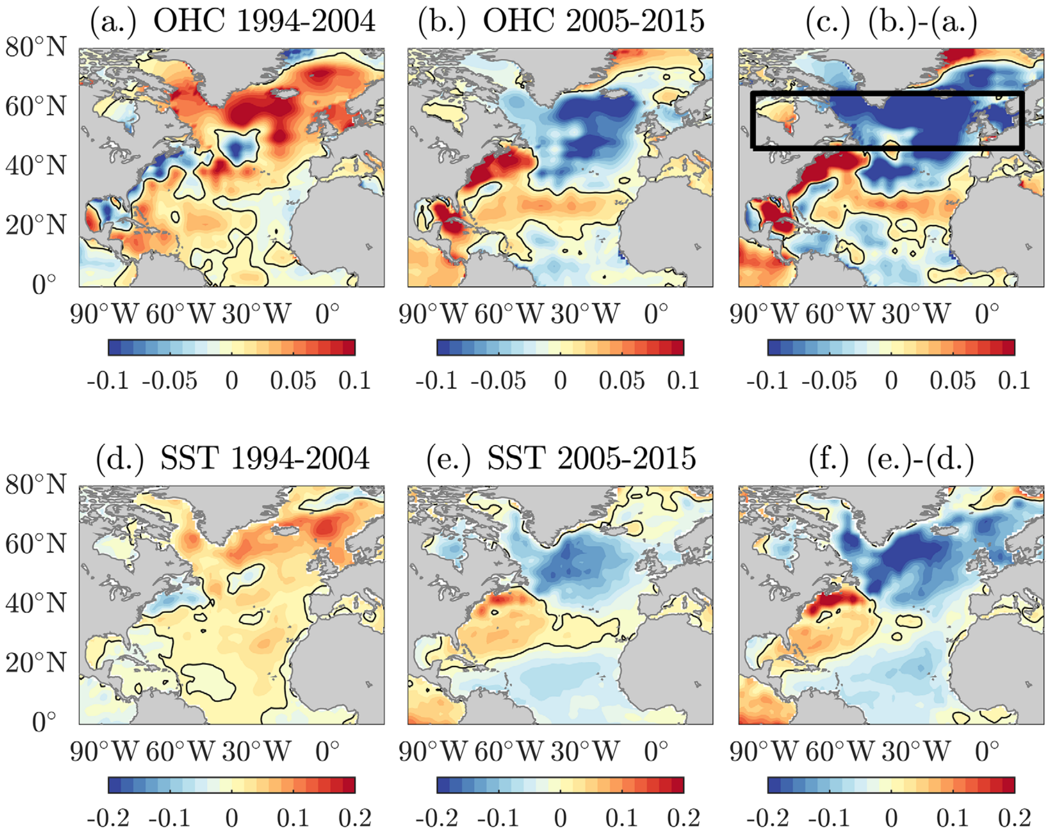

Figure 1. Linear trend in Met Office Hadley Centre EN4.2.0 ocean heat content (top 700 m; OHC) [*Good et al.*, 2013] during (a) 1994–2004, (b) 2005–2015, and (c) difference between Figures 1b and 1a. Thick black outlined box delineates the SPNA control volume. Linear trend in NOAA Optimum Interpolation SST Version 2 sea-surface temperature [*Reynolds et al.*, 2002] during (d) 1994–2004, (e) 2005–2015, and (f) difference between Figures 1e and 1d. To emphasize regional behavior, respective global mean OHC or SST time series have been removed at each spatial grid point prior to trend calculations. Thin black contours are zero crossings. All panels have units of °C yr^{-1}.

trend reversal was not due to local Ekman pumping or surface heat exchanges. Rather, judging from declining seawater densities seen in the central Labrador Sea since around 1995 and lagged correlations between central Labrador Sea density and Atlantic meridional overturning circulation (AMOC) stream function at 40°N in a climate model, R16 hypothesize that the SPNA decadal trend reversal around 2004–2005 was related to a decline in AMOC strength [cf. also *Robson et al.*, 2014].

The interpretation of R16 is consistent with some past works (based largely on correlational analysis of climate models) concluding that SPNA decadal and multidecadal changes are linked to variations in meridional heat transport (MHT) by the AMOC, such that warmer conditions across the SPNA correspond to an increase in MHT [e.g., *Delworth et al.*, 1993; *Delworth and Greatbatch*, 2000; *Delworth and Mann*, 2000; *Latif et al.*, 2007; *Dong and Sutton*, 2005; *Knight et al.*, 2005; *Msadek and Frankignoul*, 2009; *Delworth and Zeng*, 2012; *Roberts et al.*, 2013]. It also dovetails with the emerging paradigm of a negative internal feedback mechanism thought to act on decadal time scales [*Menary et al.*, 2015; *Haine*, 2016]. Within this paradigm, anomalous midlatitude ocean circulation introduces temperature and salinity anomalies into the SPNA, which are then brought cyclonically around the SPNA gyre and into the Labrador Sea, where they impact water-column stability and water mass formation; thereafter, these density anomalies are communicated southward along the western boundary, affecting dynamic-height gradients and changing the midlatitude thermal-wind balance; the resulting geostrophic circulation anomalies flux anomalous temperatures and salinities of the opposite sign into the SPNA, thus reversing the initial process [e.g., see *Menary et al.*, 2015, Figure 9].

Yet correlation between decadal SPNA SST and OHC changes and shifts in the AMOC need not necessarily imply that the latter is the foremost causal driver of the former, and other processes might be relevant to recent SPNA temperature trend reversals. While AMOC renders dominant contributions to tropical and subtropical Atlantic MHT, other flows are integral at other latitudes. For example, at middle and higher latitudes in the Atlantic, horizontal gyre circulations can contribute as much—if not more—to MHT than AMOC, reflecting decreased vertical temperature gradients, increased horizontal temperature gradients, and a more barotropic flow regime compared to lower latitudes [e.g., *Dong and Sutton*, 2001; *Jayne and Marotzke*, 2001; *Shaffrey and Sutton*, 2004; *Marsh et al.*, 2008; *Grist et al.*, 2010; *Ferrari and Ferreira*, 2011; *Piecuch and Ponte*, 2012]. Wind stress changes can lead to expansion or contraction of the North Atlantic gyres, and concomitant eastward or westward migration of the subpolar front, allowing the increased or decreased intrusion of warmer, saltier subtropical waters into the cooler, fresher subpolar regions on decadal periods [e.g., *Marshall et al.*, 2001; *Häkkinen and Rhines*, 2004, 2009; *Hátún et al.*, 2005; *Brambilla and Talley*, 2006; *Lozier and Stewart*, 2008; *Burkholder and Lozier*, 2011; *Häkkinen et al.*, 2011a,2011b,2013; *Zhai and Sheldon*, 2012; *Barrier et al.*, 2014, 2015]. In fact, numerous studies focusing on the warming of the SPNA in the 1990s implicated changes in gyre circulation resulting from changes in the wind stress related to the North Atlantic Oscillation or atmospheric blocking [e.g., *Bersch*, 2002; *Lozier and Stewart*, 2008; *Sarafanov et al.*, 2008; *Häkkinen et al.*, 2011a,2013]. Accordingly, the basic nature of the recent trend reversal—whether forced locally or remotely, driven by winds or buoyancy, sustained by an internal ocean mechanism or coupled to the overlying atmosphere, tied to overturning or gyre circulations—remains to be clarified.

Here we seek to illuminate the recent decadal changes in SPNA OHC. To this end, we consider a new (version 4) global ocean state estimate produced by the Estimating the Circulation and Climate of the Ocean consortium (ECCOv4) [*Forget et al.*, 2015]. The remainder of the paper is structured as follows: in section 2, we describe the ocean state estimate and compare it to observational data; in section 3, we present our main findings, including comprehensive diagnosis of the SPNA heat budget; in section 4, we summarize and discuss our findings.

2. Methods

2.1. Ocean State Estimate

ECCOv4 is a new-generation estimate of the global ocean circulation and sea-ice state since 1992—a physically consistent synthesis of a state-of-the-science general circulation model and most extant ocean data, generated using advanced inverse techniques [*Wunsch and Heimbach*, 2007; *Wunsch et al.*, 2009; *Forget et al.*, 2015]. The general estimation framework is described in detail elsewhere [*Forget et al.*, 2015], and a short description suffices for the present purposes. The solution is generated by a global general circulation model [*Marshall et al.*, 1997], which includes the Arctic Ocean as well as sea-ice and snow submodels, and is defined on a spatial grid with 1° nominal horizontal resolution and 50 layers in the vertical. Standard parameterizations are employed to represent unresolved small-scale effects [*Redi*, 1982; *Gent and McWilliams*, 1990; *Gaspar et al.*, 1990]. Through the adjoint method [*Heimbach et al.*, 2005], initial conditions, atmospheric boundary conditions, and some model parameters are iteratively adjusted to bring the model solution into consistency with the available observations to within prior uncertainty estimates. Surface heat and freshwater forcing is based on bulk formulae, with the initial guesses for the atmospheric state taken from the European Centre for Medium-Range Weather Forecasts Reanalysis-Interim (ERA-Interim) [*Dee et al.*, 2011]. For surface momentum forcing, wind stress is prescribed directly, with the initial guesses again from ERA-Interim. While constrained to data, the solution retains physical consistency, obeying conservation rules coded into the model, for instance, allowing closed heat budget analysis [*Piecuch and Ponte*, 2012; *Buckley et al.*, 2014, 2015; *Thompson et al.*, 2016]. Here we use the latest "Release 3" of the ECCOv4 solution. Differences relative to the ECCOv4 Release 1 product described by *Forget et al.* [2015] include extension through 2015 and incorporation of Gravity Recovery and Climate Experiment (GRACE) retrievals. Due to the comparatively fewer data constraints in 1992 (e.g., only partial satellite altimetric coverage), we consider the solution over 1993–2015.

2.2. Comparison to Observations

To evaluate the realism of the estimate, we compare to data. We consider SST from the National Oceanic and Atmospheric Administration (NOAA) Optimum Interpolation SST Version 2 [*Reynolds et al.*, 2002]. This data set is an optimum interpolation of in situ and satellite SST measurements, intended for analysis of climate. Global 1° monthly SST maps were retrieved from NOAA on 24 October 2016.

We use OHC from the Met Office Hadley Centre EN4.2.0 product [*Good et al*., 2013]. The version of the data used here has the *Gouretski and Reseghetti* [2010] bias corrections applied. This product represents an objective analysis of various quality controlled ocean temperature and salinity profile data sets (e.g., World Ocean Database, Arctic Synoptic Basin Wide Oceanography project, Global Temperature and Salinity Profile Program, Argo). Gridded 1° monthly temperature data with 42 levels were taken from Met Office Hadley Centre on 24 October 2016. We calculate upper OHC by integrating temperature grids over the top 700 m and full-depth OHC by integrating over the entire water column. Values are scaled by specific heat capacity times the density of seawater.

We compare ECCOv4 to observations over the SPNA, defined here as the North Atlantic between 46°N and 65°N (cf., Figure 1c). This definition is motivated by the desire to capture the spatially coherent SST and OHC trend reversals concentrated in this area, but so as not to capture the prominent trend reversals of the opposite sign in the subtropical region roughly over the Gulf Stream. (More discussion of the choice of the control volume, and sensitivity of results to control-volume choice, follows below.) Here we are interested in the overall changes integrated over the volume, rather than in the details of the spatial distribution of changes within the region. Also, to emphasize decadal variability, here and throughout the paper we remove linear trends and seasonal cycles from all time series.

The state estimate is a good fit to the available SPNA SST and OHC data. It reproduces observed large-scale trend reversals with high fidelity, and more generally explains 93%, 86%, and 78% of the total nonsecular, nonseasonal monthly SPNA SST, upper OHC, and full-depth OHC data variance, respectively, during 1993–2015 (Figure 2), where we define the variance in series x explained by series y as

$$100\% \times \left[1 - \frac{\sigma^2(x-y)}{\sigma^2(x)}\right], \tag{1}$$

where σ^2 is variance. As shown in the supporting information, ECCOv4 is also a good fit to variable sea-surface height from satellite altimetry, ocean-bottom pressure from satellite gravity, and the meridional overturning circulation from a moored array at 26°N in the Atlantic (supporting information Text S1 and

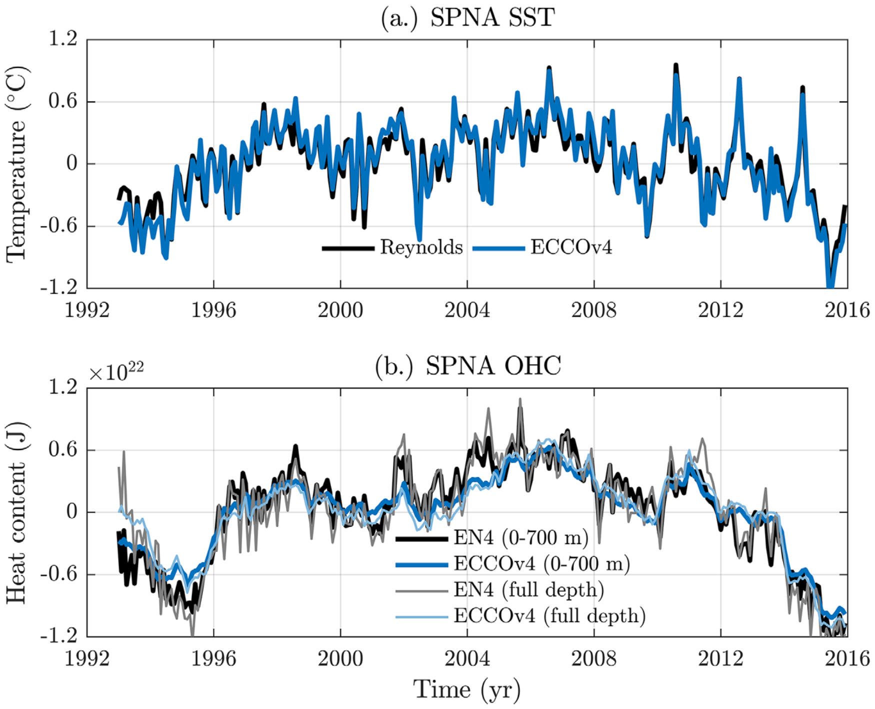

Figure 2. (a) SST from NOAA Optimum Interpolation SST Version 2 observations [*Reynolds et al*., 2002] (black) and ECCOv4 (blue) averaged over the SPNA. (b) OHC from Met Office Hadley Centre EN4.2.0 observations [*Good et al*., 2013] (black) and ECCOv4 (blue) over the SPNA. Thick dark lines represent OHC integrated over the top 700 m while thin pale lines represent OHC integrated over the full water column depth. To emphasize decadal anomalies, all time series have been detrended and seasonally adjusted.

supporting information Figures S1 and S2). Major mean North Atlantic circulation features in ECCOv4, summarized by barotropic and overturning stream functions, are displayed in supporting information Figure S3 and discussed in supporting information Text S2.

Comparisons in supporting information Figures 2 and supporting information S1 are not truly independent, since the state estimate is constrained to some of the same data. Nevertheless, these results (along with supporting information Figures S2 and S3) provide confidence in the realism of the state estimate. Importantly, the ECCOv4 solution provides a complete, physically consistent description of the ocean beyond what is measured, useful for inferring causal mechanisms of the observed variations.

Table 1. Common Notation in the Text[a]

Symbol	Description
$\mathcal{A}$	Advection by ocean circulation (budget term)
$\mathcal{F}$	Forcing by surface heat exchanges (budget term)
$\mathcal{M}$	Diffusion by parameterized mixing (budget term)
$\mathcal{T}$	Total ocean heat content (budget term)
A_S	Southern-boundary area of SPNA control region
A_N	Northern boundary area of SPNA control region
V	Volume of SPNA control region
$\nabla\times\tau$	Vertical component of wind stress curl
v	Resolved (Eulerian) meridional velocity
θ	Potential temperature
t	Time
λ	Longitude
ϕ	Latitude
z	Depth
$I(\cdot)$	Time integral
$\Delta[\cdot]$	Decadal trend reversal
$(\cdot)^N$	Component at SPNA northern boundary
$(\cdot)^S$	Component at SPNA southern boundary
$(\cdot)_n$	Zonally symmetric barotropic component
$(\cdot)_v$	Zonally symmetric baroclinic component
$(\cdot)_d$	Deep and intermediate zonally symmetric baroclinic component
$(\cdot)_s$	Shallow zonally symmetric baroclinic component
$(\cdot)_h$	Horizontally asymmetric component
$(\cdot)'$	Time anomaly indicator
$\overline{(\cdot)}$	Time mean indicator
$(\cdot)^*$	Dummy variable indicator

[a]See text for details and definitions where applicable.

3. Mechanisms of the SPNA Trend Reversal Based on the ECCOv4 Estimate

What is responsible for the recent SPNA trend reversal (Figure 2)? We take advantage of the consistency and detailed model diagnostics furnished by the state estimate to address this topic, painting a detailed portrait of the relevant physics at play.

3.1. Diagnosing the Heat Budget and Quantifying the Trend Reversal

3.1.1. Heat Budget

To identify basic processes controlling SPNA thermal variations (Figure 2), we diagnose the SPNA heat budget using ECCOv4. Changes in the heat content of an oceanic control volume can be caused by convergences and divergences of advective, diffusive, and surface heat fluxes within the control volume. To concentrate on exchanges with the atmosphere and adjacent ocean regions, and avoid considering the effects of local vertical heaving, we focus on the budget for the total OHC, integrating from the sea surface to ocean bottom. In addition, we choose a control volume that extends longitudinally to the North American and European continents, encompassing portions of Hudson Bay, the North Sea, and the Greenland, Iceland, Norwegian Seas (Figure 1c). This decision was made to simplify the form of the budget, such that zonal fluxes between the open ocean and marginal seas need not be considered. However, ECCOv4 SPNA thermal variations are mostly confined to the upper layer, and the volume of these marginal seas is comparatively small, so the total integrated SPNA OHC is minimally impacted by the deep ocean (below 700 m) or these marginal seas, and hence the results of our analyses are insensitive to these choices (cf., Figure 2b).

The budget for total OHC changes over the SPNA can be written as

$$\underbrace{c_p\rho_0\int_t\iiint_V\frac{\partial\theta}{\partial t}dV^*dt^*}_{\mathcal{T}}=\underbrace{c_p\rho_0\int_t\iiint_V[-\nabla\cdot(\vec{u}_{res}\theta)]dV^*dt^*}_{\mathcal{A}}+\underbrace{c_p\rho_0\int_t\iiint_V D_\theta\,dV^*dt^*}_{\mathcal{M}}$$
$$+\underbrace{c_p\rho_0\int_t\iiint_V F_\theta\,dV^*dt^*}_{\mathcal{F}}. \quad (2)$$

Here θ is potential temperature, c_p is specific heat capacity, ρ_0 is a reference density of seawater, t is time, V is volume, and $\vec{u}_{res}\equiv(u_{res},v_{res},w_{res})$ are the zonal, meridional, and vertical components of the residual

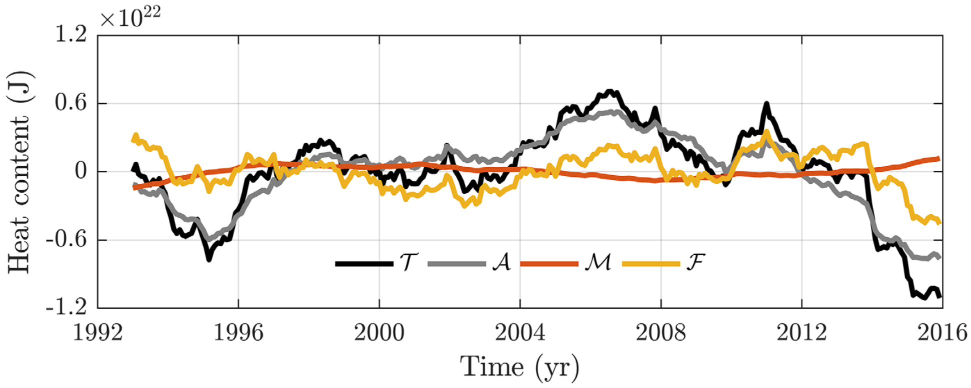

Figure 3. Full-depth ocean heat content (OHC) budget for the SPNA. Total OHC ($\mathcal{T}$; black) along with advection ($\mathcal{A}$; gray), diffusion ($\mathcal{M}$; red), and forcing ($\mathcal{F}$; yellow) budget contributions.

mean velocity, respectively; F_θ represents the net (turbulent and radiative) surface heat flux, while D_θ represents the parameterized (iso-neutral and dia-neutral) mixing. Capitalized scripted terms $\mathcal{T}$, $\mathcal{A}$, $\mathcal{M}$, and $\mathcal{F}$ (which symbolize the change in total ocean heat content, advective heat convergence, diffusive heat convergence, and surface forcing terms, respectively) have units of Joules. Asterisk denotes dummy variable (Table 1 lists our notation conventions).

Time series of budget terms, diagnosed independently using appropriate model output [cf. *Forget et al.*, 2015], are displayed in Figure 3. The budget closes exactly, such that the residual difference between left-hand and right-hand sides of equation (2) vanishes to machine precision (not shown). $\mathcal{A}$ explains 87% of the total $\mathcal{T}$ variance, the former showing similar decadal behavior to the latter, increasing over 1994–2004, and decreasing over 2005–2015 (Figure 3). $\mathcal{F}$ is relevant for some periods on interannual time scales, explaining a modest percentage of the overall $\mathcal{T}$ variance (37%), but appears relatively unimportant over the decadal time scales of main interest here (Figure 3). $\mathcal{M}$ contributes negligibly to the $\mathcal{T}$ changes (Figure 3).

3.1.2. Trend Reversal

To focus on decadal changes more specifically, we evaluate the $\mathcal{T}$ trend reversal and its $\mathcal{A}$, $\mathcal{M}$, and $\mathcal{F}$ contributions. Noting that the $\mathcal{T}$ time series has a strong quadratic nature, with an inflection point near 2004–2005, we use ordinary least squares to fit second-order polynomials to the different budget time series. For each $\mathcal{Y} \in \{\mathcal{T}, \mathcal{A}, \mathcal{M}, \mathcal{F}\}$, we determine the set of constant coefficients $\{a[\mathcal{Y}], b[\mathcal{Y}], c[\mathcal{Y}]\}$ that minimizes the residual,

$$\epsilon[\mathcal{Y}] = \mathcal{Y} - \left(a[\mathcal{Y}]t^2 + b[\mathcal{Y}]t + c[\mathcal{Y}]\right). \tag{3}$$

Table 2. Decadal Trend Reversals (TW) in Various Heat Budget Terms With Associated *p*-Values[a]

Term	Trend Reversal Δ (TW)	*p*-Value
$\mathcal{T}$	−**52.1**	**0.06**
$\mathcal{A}$	−**51.8**	**0.03**
$\mathcal{M}$	−0.1	1.00
$\mathcal{F}$	−0.2	0.99
$\mathcal{A}^S$	−**42.7**	**0.10**
$\mathcal{A}^S_b$	−**7.3**	**0.03**
$\mathcal{A}^N$	**15.7**	**0.03**
$\mathcal{A}^N_b$	2.9	0.21
$\mathcal{A}^S\{v_n\theta_n\}$	0.7	0.32
$\mathcal{A}^S\{v_h\theta_h\}$	−**51.8**	**0.05**
$\mathcal{A}^S\{v_v\theta_v\}$	9.5	0.45
$\mathcal{A}^S\{v_s\theta_s\}$	9.8	0.44
$\mathcal{A}^S\{v_d\theta_d\}$	−0.40	0.79
$\mathcal{A}^S\{\overline{v_h}\theta'_h\}$	10.8	0.42
$\mathcal{A}^S\{v'_h\overline{\theta_h}\}$	−61.5	0.12
$\mathcal{A}^S\{v'_h\theta'_h\}$	−1.00	0.41

[a] Statistically significant values ($p \leq 0.10$) are indicated with bold font. According to the conventions in equation (4), negative Δ values indicate a positive trend followed by a negative trend.

To assess significance of the estimators (*p*-values), we use a phase-scrambling method detailed in supporting information Text S3. Using these estimators, we define the decadal $\mathcal{Y}$ trend reversal as

$$\Delta[\mathcal{Y}] \doteq a[\mathcal{Y}]\delta t,$$

where $\delta t = 23$ year is the duration of the 1993–2015 study period. This approach for defining the trend reversal is robust; similar results follow from taking the difference between trends computed during 2005–2015 and 1994–2004 (not shown). Throughout the paper, we quote most $\Delta[\mathcal{Y}]$ values in units of TW ($1\ \mathrm{TW} = 10^{12}\ \mathrm{W} \approx 3.2 \times 10^{19}\ \mathrm{J\ yr^{-1}}$).

Estimated trend reversals are tabulated in Table 2. $\Delta[\mathcal{T}]$ and $\Delta[\mathcal{A}]$ are very similar and both statistically significant. In contrast, $\Delta[\mathcal{F}]$ and $\Delta[\mathcal{M}]$ are much smaller in magnitude and indistinguishable from zero. These results demonstrate that the recent SPNA decadal trend reversal was mostly owing to advective convergences by ocean circulation, which is consistent with our foregoing visual assessment of the time series in Figure 3; these results also agree with conclusions drawn more broadly in previous studies regarding the relative roles of ocean advection and surface heat flux forcing in controlling SPNA heat content on decadal time scales [*Grist et al*., 2010; *Williams et al*., 2014; *Menary et al*., 2015; R16].

3.2. Decomposing Advection

3.2.1. Eulerian and Bolus Contributions at Southern and Northern Boundaries

To further elucidate the $\mathcal{A}$ contributions that are largely responsible for $\Delta[\mathcal{T}]$, we break $\mathcal{A}$ down into its component parts owing to resolved (Eulerian) and parameterized (bolus) circulation across the region's southern and northern boundaries, applying the divergence theorem, whence,

$$\begin{aligned}\mathcal{A} &\doteq c_p\rho_0\int_t\iiint_V[-\nabla\cdot(\vec{u}_{res}\theta)]dV^*dt^*\\ &= \underbrace{c_p\rho_0\int_t\iint_{A_S}(-v\theta)dA^*dt^*}_{\mathcal{A}^S}+\underbrace{c_p\rho_0\int_t\iint_{A_S}(-v_b\theta)dA^*dt^*}_{\mathcal{A}_b^S}.\\ &\quad+\underbrace{c_p\rho_0\int_t\iint_{A_N}(v\theta)dA^*dt^*}_{\mathcal{A}^N}+\underbrace{c_p\rho_0\int_t\iint_{A_N}(v_b\theta)dA^*dt^*}_{\mathcal{A}_b^N}\end{aligned}\qquad(4)$$

Here A_S and A_N are southern and northern boundary area, respectively, while v and v_b are meridional Eulerian and bolus velocity, respectively; $\mathcal{A}^S$ and $\mathcal{A}_b^S$ are thus contributions from resolved and parameterized advection over the southern boundary, respectively, and $\mathcal{A}^N$ and $\mathcal{A}_b^N$ are similarly Eulerian and bolus advection at the northern boundary.

Time series of advection components in equation (4) are shown in Figure 4. $\mathcal{A}$ changes are predominantly owing to $\mathcal{A}^S$, such that $\mathcal{A}^S$ explains 96% of the variance in $\mathcal{A}$ (Figure 4). Accordingly, the overall contributions from $\mathcal{A}^N$, $\mathcal{A}_b^S$, and $\mathcal{A}_b^N$ are relatively less important in comparison (Figure 4). We note that, despite their different magnitudes, $\mathcal{A}^S$ and $\mathcal{A}^N$ are anticorrelated and compensate one another (correlation coefficient of -0.93). This result reflects coherence between resolved meridional flows at 46°N and 65°N (not shown). In terms of trend reversals, the value for $\Delta[\mathcal{A}^S]$ is very close to the value for $\Delta[\mathcal{A}]$ (Table 2). However, values for $\Delta[\mathcal{A}_b^S]$, $\Delta[\mathcal{A}^N]$, and $\Delta[\mathcal{A}_b^N]$, while smaller, are not totally negligible. Indeed, $\Delta[\mathcal{A}^N]$ and $\Delta[\mathcal{A}_b^S]$ are both distinguishable from zero, suggesting minor albeit significant contributions from small-scale midlatitude ocean processes as well as large-scale ocean processes at higher latitudes.

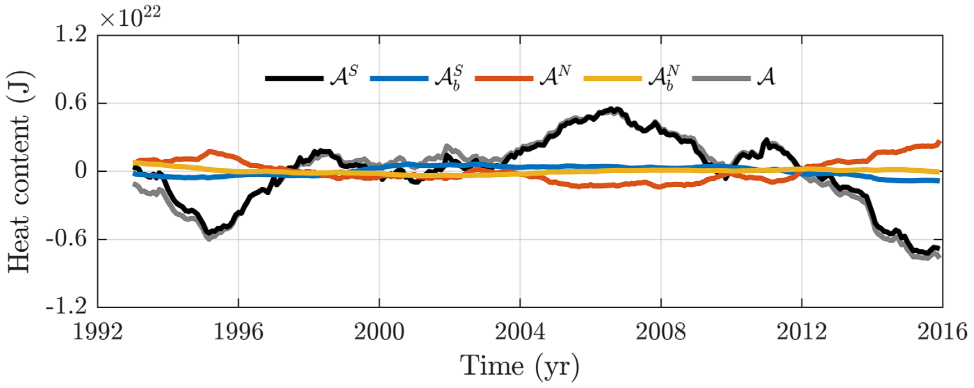

Figure 4. Decomposition of advection ($\mathcal{A}$; gray) into contributions from resolved (large-scale Eulerian) advection at 46°N [$\mathcal{A}^S$; black], parameterized (small-scale bolus) advection at 46°N [$\mathcal{A}_b^S$; blue], resolved advection at 65°N [$\mathcal{A}^N$; red], and parameterized advection at 65°N [$\mathcal{A}_b^N$; yellow].

3.2.2. Spatial Decomposition of Southern-Boundary Eulerian Advection

To reveal the nature of the $\mathcal{A}^S$ changes that render the foremost contributions to $\Delta[\mathcal{T}]$ (Figures 3 and 4), we use established kinematic decompositions [e.g., *Peixoto and Oort*, 1992; *Bryden and Imawaki*, 2001]. First, we partition $\mathcal{A}^S$ in space (longitude and depth), evaluating zonally symmetric barotropic, zonally symmetric baroclinic, and zonally asymmetric contributions, *viz.*,

$$\begin{aligned}\mathcal{A}^S &\doteq c_p\rho_0\int_t\iint_{A_S}(-v\theta)dA^*dt^*\\ &= \underbrace{c_p\rho_0\int_t\iint_{A_S}(-v_n\theta_n)dA^*dt^*}_{\mathcal{A}^S\{v_n\theta_n\}}+\underbrace{c_p\rho_0\int_t\iint_{A_S}(-v_v\theta_v)dA^*dt^*}_{\mathcal{A}^S\{v_v\theta_v\}}\\ &\quad+\underbrace{c_p\rho_0\int_t\iint_{A_S}(-v_h\theta_h)dA^*dt^*}_{\mathcal{A}^S\{v_h\theta_h\}},\end{aligned}\tag{5}$$

where

$$v_n(\phi,t)\doteq\int_z\int_\lambda v(\lambda^*,\phi,z^*,t)\,d\lambda^*\,dz^*\Big/\int_z\int_\lambda d\lambda^*\,dz^*,\tag{6}$$

$$v_v(\phi,z,t)\doteq\int_\lambda[v(\lambda^*,\phi,z,t)-v_n(\phi,t)]\,d\lambda^*\Big/\int_\lambda d\lambda^*,\tag{7}$$

$$v_h(\lambda,\phi,z,t)\doteq v(\lambda,\phi,z,t)-v_n(\phi,t)-v_v(\phi,z,t),\ (\lambda,z)\in A_S,\tag{8}$$

where λ and ϕ are longitude and latitude, respectively. (A similar partition is done for θ.) Thus defined, $\mathcal{A}^S\{v_n\theta_n\}$ is advection corresponding to net volume transport, $\mathcal{A}^S\{v_v\theta_v\}$ advection due to vertical overturning circulations, and $\mathcal{A}^S\{v_h\theta_h\}$ advection by horizontal gyre circulations, all across the southern boundary.

Since it accounts for vertical overturning circulations over all depths, we partition $\mathcal{A}^S\{v_v\theta_v\}$ further, separating contributions by shallow overturning from those owing to intermediate and deep overturning [cf. *Jayne and Marotzke*, 2001], *viz.*,

$$\begin{aligned}\mathcal{A}^S\{v_v\theta_v\} &\doteq c_p\rho_0\int_t\iint_{A_S}(-v_v\theta_v)dA^*dt^*\\ &= \underbrace{c_p\rho_0\int_t\iint_{A_S}(-v_s\theta_s)dA^*dt^*}_{\mathcal{A}^S\{v_s\theta_s\}}+\underbrace{c_p\rho_0\int_t\iint_{A_S}(-v_d\theta_d)dA^*dt^*}_{\mathcal{A}^S\{v_d\theta_d\}},\end{aligned}\tag{9}$$

such that,

$$v_s(\phi,z,t)\doteq v_v(\phi,z,t)H(d+z)-\frac{1}{h}\int_{-h}^{0}[v_v(\phi,z^*,t)H(d+z^*)]dz^*,\tag{10}$$

$$v_d(\phi,z,t)\doteq v_v(\phi,z,t)-v_s(\phi,z,t),\ d>0,\ h>0,\tag{11}$$

where H is the Heaviside step function. (A similar partition is done for θ.) Thus, $\mathcal{A}^S\{v_s\theta_s\}$ embodies the action of Ekman heat transports confined to a shallow surface layer (of depth d) and compensated by a barotropic return flow (uniform over ocean depth h), whereas $\mathcal{A}^S\{v_d\theta_d\}$ constitutes the remaining (mostly geostrophic) contributions from the intermediate and deep overturning. Here we choose $d = 100$ m, a choice that is discussed in more detail in supporting information Text S4 (cf. also supporting information Figure S5).

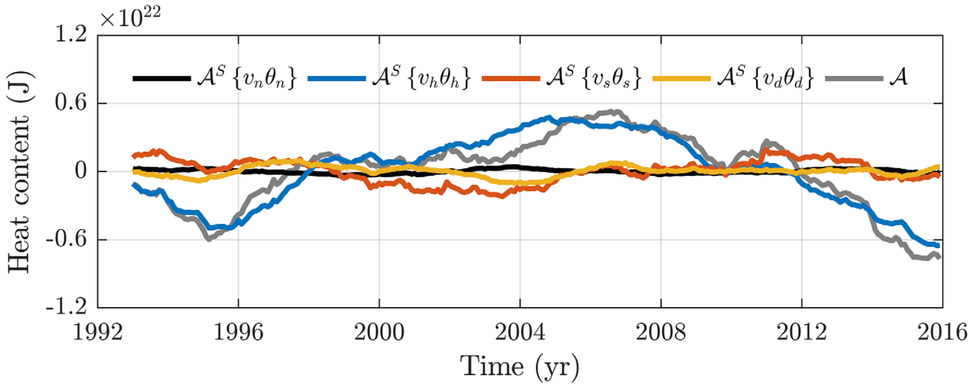

Figure 5. Contributions to $\mathcal{A}^S$ from advection due to net volume transport [$\mathcal{A}^S\{v_n\theta_n\}$; black], horizontal gyre circulations [$\mathcal{A}^S\{v_h\theta_h\}$; blue], shallow Ekman overturning [$\mathcal{A}^S\{v_s\theta_s\}$; red], and intermediate and deep overturning [$\mathcal{A}^S\{v_d\theta_d\}$; yellow]. The total advection ($\mathcal{A}$; gray) is also shown for reference.

Effects of $\mathcal{A}^S\{v_n\theta_n\}$, corresponding to southward flow in the Atlantic that balances a northward transport into the Arctic through the Bering Strait, are negligible, and $\Delta[\mathcal{A}^S\{v_n\theta_n\}]$ is vanishingly small and not distinguishable from zero (Figure 5 and Table 2). Phasing of the $\mathcal{A}^S\{v_s\theta_s\}$ time series is distinct from the $\mathcal{A}^S$ curve, such that subtracting the former from the latter actually increases (rather than decreases) variance (Figure 5). $\Delta[\mathcal{A}^S\{v_s\theta_s\}]$ is comparatively small and insignificant, suggesting that Ekman processes do not explain the recent decadal trend reversal (Table 2), consistent with R16. Similarly, variations in $\mathcal{A}^S\{v_d\theta_d\}$ due to the deeper overturning are distinct in terms of timing and amplitude compared to $\mathcal{T}$, $\mathcal{A}$, and $\mathcal{A}^S$. $\Delta[\mathcal{A}^S\{v_d\theta_d\}]$ is small, and indistinguishable from zero, revealing that changes in the deep overturning cannot account for the recent SPNA decadal changes. Rather, decadal variability during 1993–2015 is in largest part related to advection by horizontal gyres. Quantitatively, $\mathcal{A}^S\{v_h\theta_h\}$ explains 93% and 68% of variance in $\mathcal{A}^S$ and $\mathcal{T}$, respectively, and $\Delta[\mathcal{A}^S\{v_h\theta_h\}]$ amounts to $\sim$99% of $\Delta[\mathcal{T}]$ (Figure 5 and Table 2).

3.2.3. Temporal Decomposition of Horizontal Gyre Advection

Having established its primary importance (Figure 5), we now decompose $\mathcal{A}^S\{v_h\theta_h\}$ in time. Changes in $\mathcal{A}^S\{v_h\theta_h\}$ can be due to temporal anomalies in the zonally asymmetric meridional velocities, potential temperatures, or covariance between the two,

$$\begin{aligned}\mathcal{A}^S\{v_h\theta_h\} &\doteq c_p\rho_0\int_t\iint_{A_S}(-v_h\theta_h)dA^*dt^* \\ &= \underbrace{c_p\rho_0\int_t\iint_{A_S}\left(-v_h'\overline{\theta_h}\right)dA^*dt^*}_{\mathcal{A}^S\{v_h'\overline{\theta_h}\}} + \underbrace{c_p\rho_0\int_t\iint_{A_S}\left(-\overline{v_h}\theta_h'\right)dA^*dt^*}_{\mathcal{A}^S\{\overline{v_h}\theta_h'\}} \\ &\quad + \underbrace{c_p\rho_0\int_t\iint_{A_S}\left(-v_h'\theta_h'\right)dA^*dt^*}_{\mathcal{A}^S\{v_h'\theta_h'\}}\,.\end{aligned} \tag{12}$$

Here overbar and prime are time-mean and time-anomaly, respectively. Thus, $\mathcal{A}^S\{v_h'\overline{\theta_h}\}$ is horizontal gyre advection by velocity anomalies operating on mean temperatures, $\mathcal{A}^S\{\overline{v_h}\theta_h'\}$ advection by mean velocities acting on temperature anomalies, and $\mathcal{A}^S\{v_h'\theta_h'\}$ advection owing to covariance between velocity and temperature anomalies.

$\mathcal{A}^S\{v_h'\overline{\theta_h}\}$ changes make the foremost contributions to $\mathcal{A}^S\{v_h\theta_h\}$ variations, such that the former explains 90% of the variance in the latter (Figure 6). In terms of trend reversals, $\Delta[\mathcal{A}^S\{v_h'\overline{\theta_h}\}]$ is in fact larger than $\Delta[\mathcal{A}^S\{v_h\theta_h\}]$ and $\Delta[\mathcal{T}]$ (Table 2). Indeed, the action of $\mathcal{A}^S\{v_h'\overline{\theta_h}\}$ is slightly compensated by $\mathcal{A}^S\{\overline{v_h}\theta_h'\}$; although changes due to $\mathcal{A}^S\{\overline{v_h}\theta_h'\}$ are smaller than those due to $\mathcal{A}^S\{v_h'\overline{\theta_h}\}$ (Figure 6), the two time series are strongly anticorrelated (correlation coefficient of -0.90). *Buckley et al.* [2015] discuss similar instances of anticorrelation more broadly over the extratropical North Atlantic (cf. their Figures 4c and 5d).

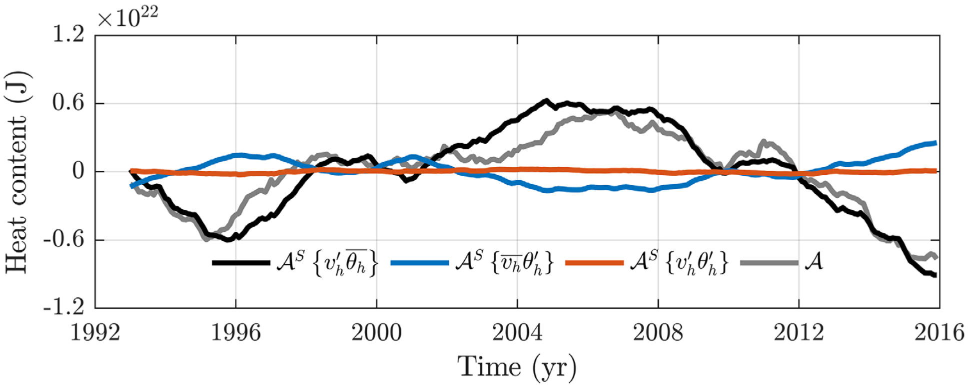

Figure 6. Contributions to $\mathcal{A}^S\{v_h\theta_h\}$ from velocity anomalies acting on mean temperatures [$\mathcal{A}^S\{v'_h\overline{\theta_h}\}$; black], mean velocities operating on anomalous temperatures [$\mathcal{A}^S\{\overline{v_h}\theta'_h\}$; blue], and covariance of velocity and temperature anomalies [$\mathcal{A}^S\{v'_h\theta'_h\}$; red]. The total advection ($\mathcal{A}$; gray) is also shown for reference.

To sum up to this point, results in Figures 3–6 and Table 2 reveal that advection due to temporal anomalies in zonally asymmetric velocities acting on time means of zonally asymmetric temperatures along the southern boundary $\left[\mathcal{A}^S\{v'_h\overline{\theta_h}\}\right]$ represent the most important contributions to the recent decadal trend reversal in the estimated SPNA heat content ($\mathcal{T}$). This motivates further study of the nature of the midlatitude horizontal gyre anomalies (v'_h) and the structure of mean temperatures ($\overline{\theta_h}$) upon which they act.

3.2.4. Nature and Structure of Advection by Anomalous Gyre Circulation

The spatial structure of $\overline{\theta_h}$ along 46°N (Figure 7a) shows relatively cooler subpolar waters to the west close to the surface, over the shelf and slope, and comparatively warmer subtropical waters to the east over a broader range of depths. A strong zonal gradient in $\overline{\theta_h}$ is evident in the upper ocean toward the west,

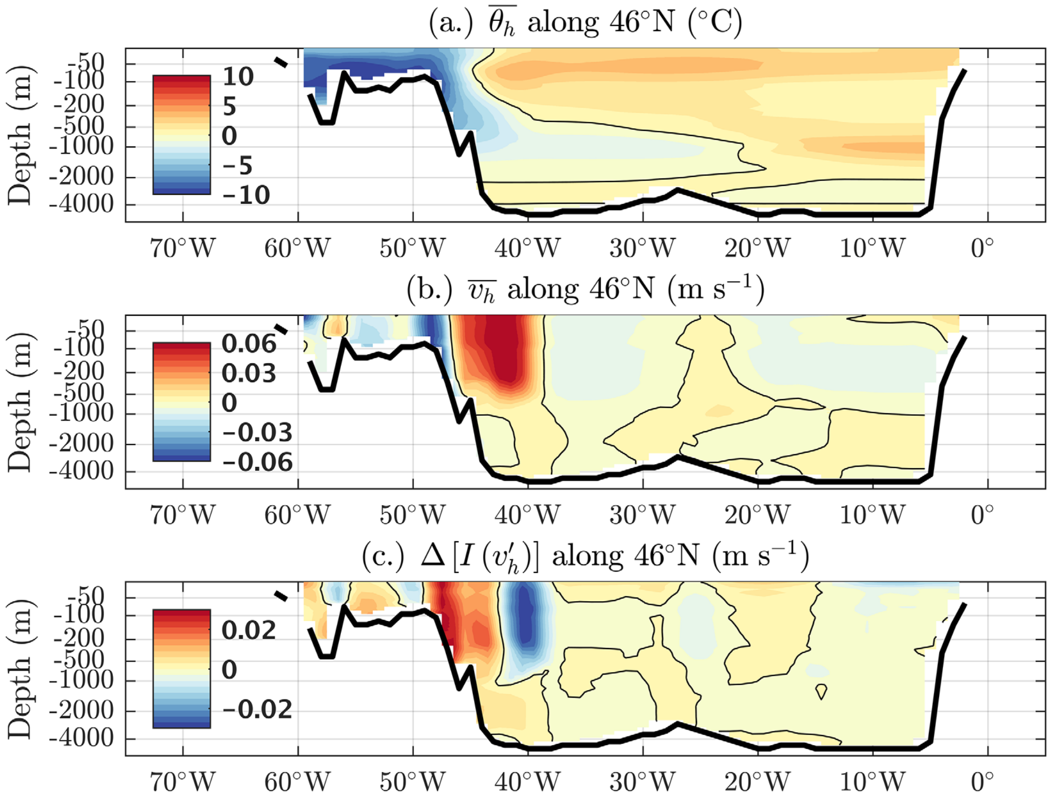

Figure 7. (a) $\overline{\theta_h}$, (b) $\overline{v_h}$, and (c) $\Delta\left[I\left(v'_h\right)\right]$ along 46°N. Thin black contours are zero crossings. Recall that $\overline{\theta_h}$ values, reaching down to −10°C in some places, are not absolute values but *spatial anomalies*.

indicating a vertically sheared, steady state meridional flow in thermal-wind balance. The sense of this current is such that transport is increasingly northward closer to the surface. Indeed, these inferences are consistent with the structure of the mean horizontal gyre meridional velocity ($\overline{v_h}$) at this latitude, which shows strong baroclinic northward flow concentrated over 40°W–45°W, and a narrower southward baroclinic current restricted to over 45°W–50°W in the upper ocean (Figure 7b), reflecting (at least in part) the northward North Atlantic and southward Labrador Currents in the model.

To illuminate the relevant circulation changes contributing to the decadal trend reversal, we consider the spatial structure of v'_h along the boundary. The most obvious feature of the $\mathcal{A}^S\{v'_h\overline{\theta_h}\}$ curve is its concave shape (Figure 6). That is, $\mathcal{A}^S\{v'_h\overline{\theta_h}\}$ values generally increase prior to 2005 and subsequently decrease thereafter (i.e., $\Delta[\mathcal{A}^S\{v'_h\overline{\theta_h}\}] < 0$). These decadal $\mathcal{A}^S\{v'_h\overline{\theta_h}\}$ changes are by definition related to decadal undulations in the *time integral* of v'_h (cf., equation (12)). For convenience, let us introduce the convention that $I(x)$ denotes the time integral of a variable x (Table 1). To understand the decadal concavity of the $\mathcal{A}^S\{v'_h\overline{\theta_h}\}$ curve, we consider $\Delta[I(v'_h)]$ over each longitude and depth along the SPNA southern boundary. (As in previous sections, Δ notation signifies decadal trend reversal, with $\Delta < 0$ corresponding to a positive trend followed by a negative trend.)

A pronounced $\Delta[I(v'_h)]$ zonal dipole is seen, concentrated in the upper 1000 m of the western North Atlantic (Figure 7c). Positive values are found to the west over the slope, reflecting a negative trend in $I(v'_h)$ over 1994–2004 and a positive trend over 2005–2015. In other words, v'_h itself increased over the western slope during the 1994–2015 period. Negative $\Delta[I(v'_h)]$ values are observed to the west over the deep ocean, signaling a positive trend in $I(v'_h)$ followed by a negative trend, hence an overall v'_h decrease over this region during the study period. This structure suggests an anomalous horizontal gyre, indicating shifts in mean meridional currents mentioned above (cf., Figures 7a and 7b). The anomalous meridional flows act on $\overline{\theta_h}$ to increasingly flux warm waters southward out and cool waters northward into the control region (Figure 7). Taking the zonal integral in the definition of $\mathcal{A}^S\{v'_h\overline{\theta_h}\}$ (equation (12)) from 35°W to 50°W, where values in Figure 7c are the strongest, rather than summing over the full zonal width of the basin, one explains 89%, 69%, and 49% of the variance of the $\mathcal{A}^S\{v'_h\overline{\theta_h}\}$, $\mathcal{A}$, and $\mathcal{T}$ time series, respectively (not shown), and $\Delta[\mathcal{A}^S\{v'_h\overline{\theta_h}\}]$ for this longitude range amounts to $\sim$53% of $\Delta[\mathcal{T}]$. These results reveal that anomalous midlatitude horizontal gyre circulations restricted to the western North Atlantic Basin make critical contributions to recent decadal variations in the SPNA.

3.3. Relation to Atmospheric Forcing

3.3.1. Maximum Covariance Analysis

It remains to isolate the mechanism(s) responsible for the v'_h variations. Basic theories of the oceanic response highlight wind stress curl ($\nabla\times\tau$) as a central driver of midlatitude ocean circulation [*Sverdrup*, 1947; *Gill*, 1982; *Luyten et al.*, 1982; *Frankignoul et al.*, 1997]. Indeed, work by *Häkkinen and Rhines* [2009] and *Häkkinen et al.* [2011a] emphasizes the role of $\nabla\times\tau$ in facilitating exchange between subtropical and subpolar North Atlantic regions. To study local covariability between gyre circulation and wind curl, we perform a maximum covariance analysis (MCA) [*Björnsson and Venegas*, 1997; *von Storch and Zwiers*, 1999]. We use singular value decomposition to extract the eigenvectors and eigenvalues from the cross-covariance matrix between $I(v'_h)$ and $I(\nabla\times\tau)$ over the SPNA southern boundary. The eigenvectors can be interpreted as $I(v'_h)$ and $I(\nabla\times\tau)$ spatial patterns corresponding to successive orthogonal modes characterizing the cross-covariance. The eigenvalues relate to the fraction of cross-covariance explained by the modes, such that leading modes explain more of the squared covariance between $I(v'_h)$ and $I(\nabla\times\tau)$. Time series characterizing the modes are evaluated by projecting the original $I(v'_h)$ and $I(\nabla\times\tau)$ fields onto their respective eigenvectors.

The gravest MCA mode explains most (97%) of the squared covariance between $I(v'_h)$ and $I(\nabla\times\tau)$. The $I(v'_h)$ MCA spatial pattern (Figure 8) bears a strong resemblance to the $\Delta[I(v'_h)]$ pattern (Figure 7c). The centers of action (areas of high variance explained) include a strong, depth-dependent zonal dipole, confined to the upper ocean in the western North Atlantic Basin, which gives way to a more diffuse and depth-independent structure, spanning the water column over the eastern Iberian Basin (Figure 8). The $I(\nabla\times\tau)$ MCA spatial pattern changes sign around 40°W (Figure 9), with centers of action and local extrema of the opposite sign to the east of 40°W over the deep Iberian Basin and to the west of 40°W over the slope and abutting the North Atlantic Basin. Less pronounced centers are evident broadly over the interior, above the (a.) $I\,(v_h')$ first MCA spatial pattern along 46°N (km)

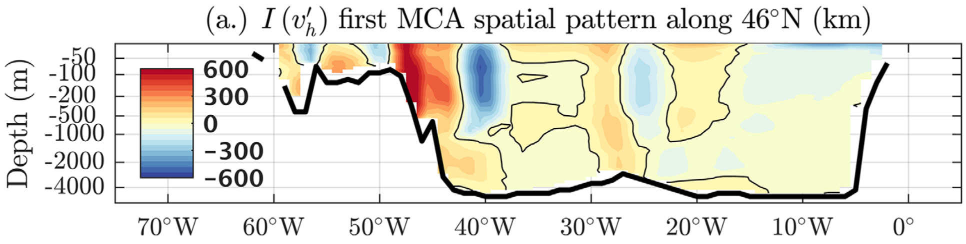

(b.) $I\,(v_h')$ variance explained by first MCA mode along 46°N (%)

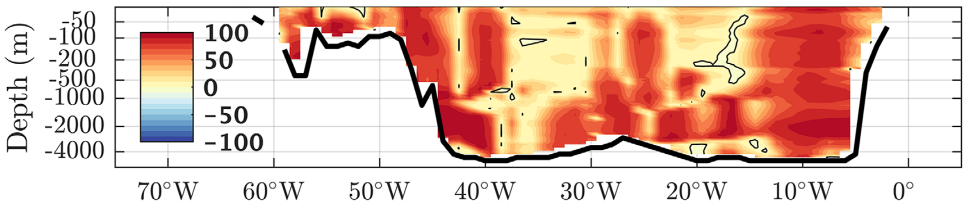

Figure 8. $I(v_h')$ (a) spatial pattern and (b) variance explained along the SPNA southern boundary at 46°N due to first MCA mode. Thin black contours are zero crossings.

Mid-Atlantic Ridge. The $I(\nabla\times\tau)$ MCA mode spatial pattern along 46°N is similar to the spatial pattern of mean $\nabla\times\tau$ at midlatitude, in that both exhibit negative values broadly west of 40°W over the deep ocean, positive values across 40°W–50°W over the continental slope, and negative values once again west of 50°W over the continental shelf (cf. Figure 9a and supporting information Figure S4). Thus, the mode of $\nabla\times\tau$ variation found here is a modulation (strengthening or weakening) of the mean midlatitude $\nabla\times\tau$ pattern.

The $I(v_h')$ and $I(\nabla\times\tau)$ MCA time series are intimately related—both are dominantly characterized by decadal undulations clearly manifested in trend reversals centered around 2004–2005 (Figure 10). The correlation coefficient between the two (0.92) is statistically significant ($p = 0.05$). (As with the trend reversals, statistical significance of correlation coefficients is evaluated based on phase scrambling as described in supporting information Text S3.) Moreover, $I(v_h')$ and $I(\nabla\times\tau)$ spatial patterns (Figures 8a and 9a), action

(a.) $I\,(\nabla\times\tau)$ first MCA spatial pattern along 46°N

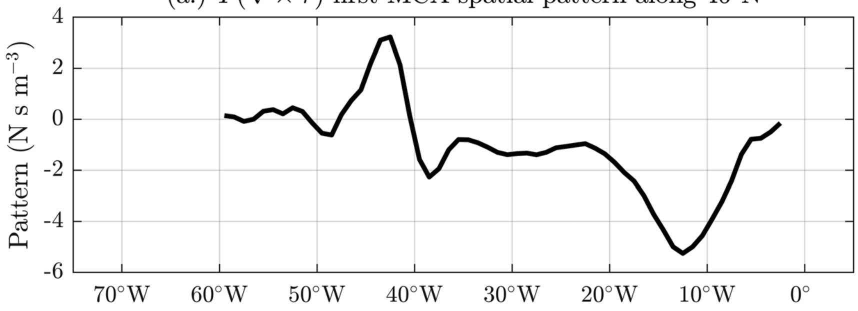

(c.) $I\,(\nabla\times\tau)$ variance explained by first MCA mode along 46°N

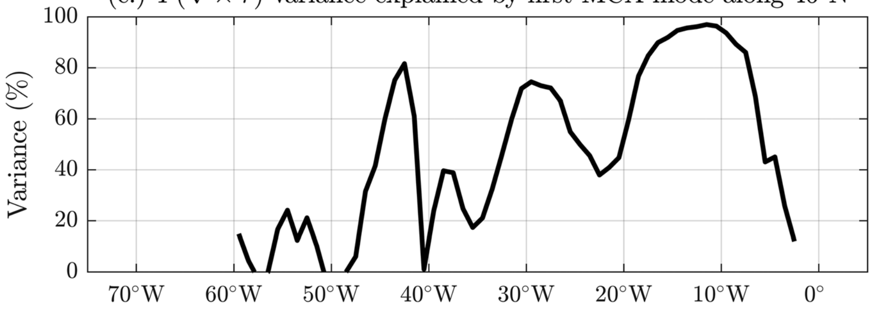

Figure 9. $I(\nabla\times\tau)$ (a) spatial pattern and (b) variance explained along the SPNA southern boundary at 46°N due to first MCA mode.

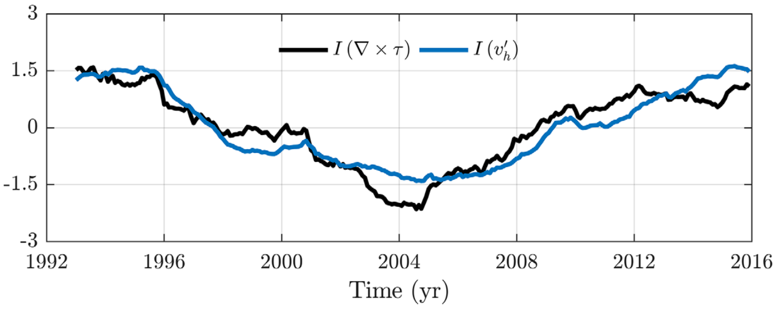

Figure 10. Time series (expansion coefficients) of $I(\nabla\times\tau)$ (black) and $I(v_h')$ (blue) of the first MCA mode. Both series have been normalized to unit variance.

centers (Figures 8b and 9b), and time series (Figure 10) from the first MCA mode are essentially identical to patterns, centers, and series found by applying empirical orthogonal function (EOF) analysis to the $I(v_h')$ and $I(\nabla\times\tau)$ fields separately (not shown), which implies that the gravest MCA mode describes covariability between the dominant modes of midlatitude $I(v_h')$ and $I(\nabla\times\tau)$ variability.

3.3.2. Dynamical Interpretation

The above results suggest a dynamical interpretation. Sverdrup theory [*Sverdrup*, 1947; *Wunsch*, 2011; *Gray and Riser*, 2014] posits that the total vertically integrated meridional volume transport per unit width (V_{Sv}) is proportional to $\nabla\times\tau$, *viz.*,

$$V_{Sv}=\frac{1}{\rho_0\beta}(\nabla\times\tau), \tag{13}$$

where ρ_0 is density and β the meridional gradient of the Coriolis parameter. Equation (13) essentially reflects vorticity balance between vertical stretching and meridional advection of the water column. From equation (13), if Sverdrup theory is a plausible mechanism for the v_h' changes, it follows that (1) v_h' and $\nabla\times\tau$ should covary in phase and share the same sign locally and (2) the ratio,

$$R\doteq\rho_0\beta Z\frac{\mathcal{O}\left[I\left(v_h'\right)\right]}{\mathcal{O}[I(\nabla\times\tau)]}, \tag{14}$$

should be order unity (where Z is a scale depth and $\mathcal{O}$ represents order of magnitude). Indeed, as noted above, $I(v_h')$ and $I(\nabla\times\tau)$ show strong in-phase covariation (Figure 10), and their centers of action and local extrema are roughly collocated in longitude, sharing the same sign (cf., negative values ~38°W and positive values ~42°W in Figures 8 and 9). Choosing reasonable values for the constants ($\rho_0\sim1000$ kg m^{-3}, $\beta\sim1.5\times10^{-11}$ m^{-1} s^{-1}, $Z\sim500$ m) and using $\mathcal{O}\left[I\left(v_h'\right)\right]\sim300$ km and $\mathcal{O}[I(\nabla\times\tau)]\sim3$ N s m^{-3} (judging from visual inspection of the western North Atlantic Basin in Figures 8 and 9), we see that in fact $R\sim1$. This suggests that the v_h' changes are roughly consistent (in terms of their phase behavior, sign, and magnitude) with the Sverdrup response anticipated given the overlying $\nabla\times\tau$ changes.

4. Summary and Discussion

We used an ocean state estimate (ECCOv4) to elucidate the origin of the recent decadal trend reversal in subpolar North Atlantic (SPNA) sea-surface temperature (SST) and ocean heat content (OHC). The state estimate reliably captures the SST and OHC decadal trend reversals seen in the observations (Figure 2). Detailed budget diagnostics show that the SPNA OHC trend reversal in the ocean state estimate is related to advection of heat by the general circulation, specifically the large-scale midlatitude transports (Figures 3 and 4). Additional spatiotemporal decompositions demonstrate that advection by horizontal gyre circulation anomalies makes primary contributions; the effects of deep and intermediate meridional overturning circulations or local surface heat flux forcing are unimportant in this context (Figures 5 and 6). The horizontal gyre advection is mainly related to a shift in the background circulation structure (Figure 7). Maximum covariance analysis (MCA) reveals that anomalous horizontal gyre circulations are intimately related to variations in the local wind stress curl (Figures 8–10), suggesting an equilibrium (Sverdrup) response. This study exemplifies the usefulness of a state estimate, whose consistency allows quantitative and comprehensive attribution of ocean behavior in terms of its underlying causal mechanisms.

While our investigation is based on analysis of a particular control volume (defined with a southern boundary at 46°N), our results relating to the SPNA heat budget are robust to the details of control volume definition. For instance, the basic nature of the SPNA heat budget is insensitive to reasonable alternative choices of the southern boundary, provided that such choices meaningfully reflect the intergyre boundary between the subtropical and subpolar gyres (cf., supporting information Text S5 and supporting information Figure S6). And while our study focused on a particular time period and spatial region, and targeted specific frequencies and wave numbers, our conclusions are in broad agreement with earlier results regarding aspects of large-scale decadal variability over the SPNA more generally.

For example, our findings have some similarities to results of *Häkkinen and Rhines* [2009] and *Häkkinen et al.* [2011a,2013] regarding the role of wind stress curl in forcing subpolar decadal variability. The mode of (integrated) wind-stress-curl variation identified here corresponds to a modulation (strengthening or weakening) of the mean midlatitude wind curl pattern (Figure 9a and supporting information Figure S4), thus bearing analogy to the "gyre mode" from Häkkinen and colleagues. The negative values $\sim$38°W and positive values $\sim$42°W related to integrated wind stress curl and horizontal gyre velocity fields in Figures 8a and 9a reflect an overall *strengthening* of the mean midlatitude wind stress curl and *weakening* of baroclinic gyre velocities over the study period, leading to progressively less warmer waters imported into and less cooler waters exported out of the region (Figures 7a and 7b), hence subpolar cooling over the latter half of the study period. This relation between the strengths of the wind stress curl and meridional heat transport is consistent with general results in *Häkkinen et al.* [2011a], namely that strengthening of the mean wind stress curl over the northern North Atlantic reduces import of warmer subtropical waters into the subpolar region. Yet our work does differ from *Häkkinen and Rhines* [2009] and *Häkkinen et al.* [2011a,2013] in terms of its emphasis—whereas Häkkinen and coauthors focus on *meridional* changes in zonal-mean wind stress curl and their impact on the strength and horizontal extent of the subtropical and subpolar gyres themselves, we highlight *zonal* variations in wind stress curl at a single latitude (46°N) and their influence on the circulation in the intergyre region between subtropical and subpolar gyres. So our study, which emphasizes the relevance of gyre circulation changes along the western intergyre region to subpolar decadal changes, complements past investigations, which have emphasized the role of the changing strength and spatial extent of the gyres themselves, and hydrographic shifts over the northeastern North Atlantic Ocean.

Our results also support the more specific argument made by *Robson et al.* [2016] (R16) that the recent SPNA decadal temperature trend reversal was not caused by Ekman heat transports or surface heat fluxes. However, our findings do not support R16's hypothesis that the recent SPNA decadal climate trend reversal was due in largest part to changes in the Atlantic meridional overturning circulation (AMOC) in lagged remote response to conditions in the Labrador Sea. (However, as discussed in supporting information Text S5, this discrepancy could partly reflect the latitudinal dependence of the meridional heat transport, and the different choices for the control volume southern boundary in the two studies.) More generally, our analysis does not preclude a role for negative internal feedbacks mechanisms involving the AMOC in SPNA decadal variability, envisioned by previous authors [e.g., *Haine*, 2016], but it does suggest that—at least for the recent decadal trend reversal—such mechanisms do not explain the observed decadal thermal variations over the SPNA.

Some caveats and shortcomings of this work should be acknowledged. Our results derive from detailed calculations performed using a particular state estimate. While representing a physically plausible and consistent embodiment of observed ocean variability, the state estimate is not provided with formal error estimates. (Methods for quantifying uncertainty in ocean state estimates are currently under development [*Kalmikov and Heimbach*, 2014].) Given the inherently evolving nature of the ocean state estimation procedure, and since elements of the ocean circulation and climate system remain poorly observed or relatively unconstrained, it cannot be ruled out that additional iterations of the state estimation could lead to different results. For example, estimates of surface air-sea heat flux can be uncertain [*Grist and Josey*, 2003; *Chaudhuri et al.*, 2013], and sustained observations of the overturning circulation in the subpolar North Atlantic have only recently commenced [*Lozier et al.*, 2017]. These considerations underscore the need for additional investigation. For instance, protocols adopted for the Ocean Model Intercomparison Project (OMIP) [*Griffies et al.*, 2016] should make such model output necessary for performing closed budget analyses much more readily available. We encourage future investigators to take advantage of these additional model diagnostics to quantify uncertainties inherent to the SPNA heat budget in ocean models.

A last caveat is that we have considered kinematic decompositions in depth coordinates (Figures 5 and 6). Alternatively, some previous studies examine meridional heat transport in density or temperature classes [*Zhang*, 2010; *Ferrari and Ferreira*, 2011; *Zika et al.*, 2012; *Xu et al.*, 2016]. Were we to consider transports in a density or temperature coordinate, rather than a depth coordinate, results would certainly point to a more dominant role for the overturning circulation. (Given the dominance of velocity variations, essentially all of the heat transport would, by definition, be related to the overturning circulation defined in temperature space, for example.) However, the tight coupling found here between local wind curl and horizontal gyre velocity suggests that remote forcing, such as variations in regions of deep convection, do not play a dominant role.

Finally, our findings have implications for decadal prediction studies. Skillful decadal climate predictions largely rely on oceanic memory and the slow (baroclinic) adjustment to initial conditions [e.g., *Keenlyside et al.*, 2008; *Dunstone et al.* 2011; *Yeager et al.*, 2012; *Roberts et al.*, 2016]. However, the picture painted by our study here is of SPNA decadal changes as the integrated equilibrium response to local wind forcing. This suggests that the predictability of the oceanic response is, in this case, tied more to the predictability of the atmospheric state than to ocean initial conditions.

Acknowledgments
Author support came from NOAA grant NA15OAR4310100 and NSF award 1513396. We acknowledge and thank Ou Wang (NASA JPL) for providing the ECCOv4 output fields needed for this analysis. More ECCO solutions are found at the group website (www.ecco-group.org/products.htm). EN4 grids are from the Met Office (http://www.metoffice.gov.uk/hadobs/en4/download-en4-2-0.html). NOAA (https://www.esrl.noaa.gov/psd/data/gridded/data.noaa.oisst.v2.html) provided the SST gridded data. The comments of two anonymous reviewers were very much appreciated and strengthened the manuscript considerably.

References

Barrier, N., C. Cassou, J. Deshayes, and A.-M. Treguier (2014), Response of North Atlantic Ocean circulation to atmospheric weather regimes, *J. Phys. Oceanogr.*, *44*, 179–201.

Barrier, N., J. Deshayes, A.-M. Treguier, and C. Cassou (2015), Heat budget in the North Atlantic subpolar gyre: Impacts of atmospheric weather regimes on the 1995 warming event, *Prog. Oceanogr.*, *130*, 75–90.

Bersch, M. (2002), North Atlantic Oscillation-induced changes of the upper layer circulation in the northern North Atlantic Ocean, *J. Geophys. Res.*, *107*(C10), 3156, doi:10.1029/2001JC000901.

Bingham, R. J., and C. W. Hughes (2009), Signature of the Atlantic meridional overturning circulation in sea level along the east coast of North America, *Geophys. Res. Lett.*, *36*, L02603, doi:10.1029/2008GL036215.

Björnsson, H., and S. A. Venegas (1997), A manual for EOF and SVD analyses of climate data, *CCGCR Rep. 97–1*, 52 pp., McGill Univ., Montreal, Canada.

Brambilla, E., and L. D. Talley (2006), Surface drifter exchange between the North Atlantic subtropical and subpolar gyres, *J. Geophys. Res.*, *111*, C07026, doi:10.1029/2005JC003146.

Bryden, H., and S. Imawaki (2001), Ocean heat transport, in *Ocean Circulation and Climate: Observing and Modelling the Global Ocean*, edited by G. Siedler, J. Church, J. Gould, pp. 455–474, Academic Press, Cambridge, U. K.

Buckley, M. W., and J. Marshall (2016), Observations, inferences, and mechanisms of the Atlantic meridional overturning circulation: A review, *Rev. Geophys.*, *54*, 5–63, doi:10.1002/2015RG000493.

Buckley, M. W., R. M. Ponte, G. Forget, and P. Heimbach (2014), Low-frequency SST and upper-ocean heat content variability in the North Atlantic, *J. Clim.*, *27*, 7503–7525.

Buckley, M. W., R. M. Ponte, G. Forget, and P. Heimbach (2015), Determining the origins of advective heat transport convergence variability in the North Atlantic, *J. Clim.*, *28*, 3943–3956.

Burkholder, K. C., and M. S. Lozier (2011), Subtropical to subpolar pathways in the North Atlantic: Deductions from Lagrangian trajectories, *J. Geophys. Res.*, *116*, C07017, doi:10.1029/2010JC006697.

Chaudhuri, A. H., R. M. Ponte, G. Forget, and P. Heimbach (2013), A comparison of atmospheric reanalysis surface products over the ocean and implications for uncertainties in air-sea boundary forcing, *J. Clim.*, *26*, 153–170.

Dee, D. P., et al. (2011), The ERA-Interim reanalysis: Configuration and performance of the data assimilation system, *Q. J. R. Meteorol. Soc.*, *137*, 553–597.

Delworth, T. L., and R. J. Greatbatch (2000), Multidecadal thermohaline circulation variability driven by atmospheric surface flux forcing, *J. Clim.*, *13*(9), 1481–1495.

Delworth, T. L., and M. Mann (2000), Observed and simulated multidecadal variability in the Northern Hemisphere, *Clim. Dyn.*, *16*, 661–676.

Delworth, T. L., and F. Zeng (2012), Multicentennial variability of the Atlantic meridional overturning circulation and its climatic influence in a 4000 year solution of the GFDL CM2.1 climate model, *Geophys. Res. Lett.*, *39*, L13702, doi:10.1029/2012GL052107.

Delworth, T. L., S. Manabe, and R. J. Stouffer (1993), Interdecadal variations of the thermohaline circulation in a coupled ocean-atmosphere model, *J. Clim.*, *6*(11), 1993–2011.

Dong, B., and R. T. Sutton (2005), Mechanism of interdecadal thermohaline circulation variability in a coupled ocean-atmosphere GCM, *J. Clim.*, *18*, 1117–1135.

Dong, B.-W., and R. T. Sutton (2001), The dominant mechanisms of variability in Atlantic ocean heat transport in a coupled ocean-atmosphere GCM, *Geophys. Res. Lett.*, *28*(12), 2445–2445.

Dunstone, N., D. Smith, and R. Eade (2011), Multi-year predictability of the tropical Atlantic atmosphere driven by the high latitude North Atlantic Ocean, *Geophys. Res. Lett.*, *37*, L14701, doi:10.1029/2011GL047949.

Ferrari, R., and D. Ferreira (2011), What processes drive the ocean heat transport?, *Ocean Modell.*, *38*, 171–186.

Forget, G., J.-M. Campin, P. Heimbach, C. N. Hill, R. M. Ponte, and C. Wunsch (2015), ECCO version 4: An integrated framework for non-linear inverse modeling and global ocean state estimation, *Geosci. Model Dev.*, *8*, 3071–3104.

Frajka-Williams, E., J. L. Bamber, and K. Våge, 2016, Greenland melt and the Atlantic meridional overturning circulation, *Oceanography*, *29*(4), 22–33, doi:10.5670/oceanog.2016.96.

Frankignoul, C., P. Müller, and E. Zorita (1997), A simple model of the decadal response of the ocean to stochastic wind forcing, *J. Phys. Oceanogr.*, *27*, 1533–1546.

Gaspar, P., Y. Grégoris, and J.-M. Lefevre (1990), A simple eddy kinetic energy model for simulations of the oceanic vertical mixing: Tests at station papa and long-term upper ocean study site, *J. Geophys. Res.*, *95*(C9), 16,179–16,193.

Gent, P. R., and J. C. McWilliams (1990), Isopycnal mixing in ocean circulation models, *J. Phys. Oceanogr.*, *20*, 150–155.

Gill, A. E. (1982), *Atmosphere-Ocean Dynamics*, 662 pp., Academic, San Diego, Calif.

Good, S. A., M. J. Martin, and N. A. Rayner (2013), EN4: Quality controlled ocean temperature and salinity profiles and monthly objective analyses with uncertainty estimates, *J. Geophys. Res. Oceans*, *118*, 6704–6716, doi:10.1002/2013JC009067.

Gouretski, V., and F. Reseghetti (2010), On depth and temperature biases in bathythermograph data: Development of a new correction scheme based on analysis of a global ocean database, *Deep Sea Res., Part I*, *57*, 6, doi:10.1016/j.dsr.2010.03.011.

Gray, A. R., and S. C. Riser (2014), A global analysis of Sverdrup balance using absolute geostrophic velocities from Argo, *J. Phys. Oceanogr.*, *44*, 1213–1229.

Griffies, S. M., et al. (2016), OMIP contribution to CMIP6: Experimental and diagnostic protocol for the physical component of the Ocean Model Intercomparison Project, *Geosci. Model Dev.*, *9*, 3231–3296, doi:10.5194/gmd-9-3231-2016.

Grist, J. P., and S. A. Josey (2003), Inverse Analysis adjustment of the SOC air-sea flux climatology using ocean heat transport constraints, *J. Clim.*, *16*, 3274–3295.

Grist, J. P., S. A. Josey, R. Marsh, S. A. Good, A. C. Coward, B. A. de Cuevas, S. G. Alderson, A. L. New, and G. Madec (2010), The roles of surface heat flux and ocean transport convergence in determining Atlantic Ocean temperature variability, *Ocean Dyn.*, *60*, 771–790, doi: 10.1007/s10236-010-0292-4.

Haine, T. W. N. (2016), Vagaries of Atlantic overturning, *Nat. Geosci.*, *9*, 479–480.

Häkkinen, S., and P. B. Rhines (2004), Decline of subpolar North Atlantic circulation during the 1990s, *Science*, *304*, 555–559.

Häkkinen, S., and P. B. Rhines (2009), Shifting surface currents in the northern North Atlantic Ocean, *J. Geophys. Res.*, *114*, C04005, doi: 10.1029/2008JC004883.

Häkkinen, S., P. B. Rhines, and D. L. Worthen (2011a), Warm and saline events embedded in the meridional circulation of the northern North Atlantic, *J. Geophys. Res.*, *116*, C03006, doi:10.1029/2010JC006275.

Häkkinen, S., P. B. Rhines, and D. L. Worthen (2011b), Atmospheric blocking and Atlantic multidecadal ocean variability, *Science*, *334*, 655–659.

Häkkinen, S., P. B. Rhines, and D. L. Worthen (2013), Northern North Atlantic sea surface height and ocean heat content variability, *J. Geophys. Res. Oceans*, *118*, 3670–3678, doi:10.1002/jgrc.20268.

Hátún, H., A. B. Sandø, H. Drange, B. Hansen, and H. Valdimarsson (2005), Influence of the Atlantic subpolar gyre on the thermohaline circulation, *Science*, *309*, 1841–1844.

Heimbach, P., C. Hill, and R. Giering (2005), An efficient exact adjoint of the parallel MIT General Circulation Model, generated via automatic differentiation, *Future Gen. Comput. Syst.*, *21*, 1356–1371.

Huss, M., R. Hock, A. Bauder, and M. Funk (2010), 100-Year mass changes in the Swiss Alps linked to the Atlantic Multidecadal Oscillation, *Geophys. Res. Lett.*, *37*, L10501, doi:10.1029/2010GL042616.

Jayne, S. R., and J. Marotzke (2001), The dynamics of ocean heat transport variability, *Rev. Geophys.*, *39*(3), 385–411.

Kalmikov, A. G., and. P. Heimbach (2014), A Hessian-based method for uncertainty quantification in global ocean state estimation, *SIAM J. Sci. Comput.*, *36*(5), S267–S295.

Keenlyside, N. S., M. Latif, J. Jungclaus, L. Kornblueh, and E. Roeckner (2008), Advancing decadal-scale climate prediction in the North Atlantic sector, *Nature*, *453*, 84–88.

Knight, J. R., R. J. Allan, C. K. Folland, M. Vellinga, and M. E. Mann (2005), A signature of persistent natural thermohaline circulation cycles in observed climate, *Geophys. Res. Lett.*, *32*, L20708, doi:10.1029/2005GL024233.

Knight, J. R., C. K. Folland, and A. A. Scaife (2006), Climate impacts of the Atlantic Multidecadal Oscillation, *Geophys. Res. Lett.*, *33*, L17706, doi:10.1029/2006GL026242.

Latif, M., C. W. Böning, J. Willebrand, A. Biastoch, F. Alvarez-Garcia, N. Keenlyside, and H. Pohlmann (2007), Decadal to multidecadal variability of the Atlantic MOC: Mechanisms and predictability, in *Ocean Circulation: Mechanisms and Impacts—Past and Future Changes of Meridional Overturning*, edited by A. Schmittner, J. C. H. Chiang, and S. R. Hemming, pp. 149–166, AGU, Washington, D. C., doi:10.1029/173GM11.

Lozier, M. S., and N. M. Stewart (2008), On the temporally varying northward penetration of Mediterranean overflow water and eastward penetration of Labrador Sea water, *J. Phys. Oceanogr.*, *38*, 2097–2103.

Lozier, M. S., S. Leadbetter, R. G. Williams, V. Roussenov, M. S. C. Reed, and N. J. Moore (2008), The spatial pattern and mechanisms of heat-content change in the North Atlantic, *Science*, *319*, 800–803.

Lozier, M. S., V. Roussenov, M. S. C. Reed, and R. G. Williams (2010), Opposing decadal changes for the North Atlantic meridional overturning circulation, *Nat. Geosci.*, *3*, 728–734.

Lozier, M. S., et al. (2017), Overturning in the Subpolar North Atlantic Program: A new international ocean observing system, *Bull. Am. Meteorol. Soc.*, *98*(5), 737–752.

Luyten, J. R., J. Pedlosky, and H. Stommel (1982), The ventilated thermocline, *J. Phys. Oceanogr.*, *13*, 292–309.

McCarthy, G. D., E. Frajka-Williams, W. E. Johns, M. O. Baringer, C. S. Meinen, H. L. Bryden, D. Rayner, A. Duchez, C. Roberts, and S. A. Cunningham (2012), Observed interannual variability of the Atlantic meridional overturning circulation at 26.5°N, *Geophys. Res. Lett.*, *39*, L19609, doi:10.1029/2012GL052933.

McCarthy, G. D., I. D. Haigh, J. J.-M. Hirschi, J. P. Grist, and D. A. Smeed (2015), Ocean impact on decadal Atlantic climate variability revealed by sea-level observations, *Nature*, *521*, 508–510, doi:10.1038/nature14491.

Marsh, R., S. A. Josey, B. A. de Cuevas, L. J. Redbourn, and G. D. Quartly (2008), Mechanisms for recent warming of the North Atlantic: Insights gained with an eddy-permitting model, *J. Geophys. Res.*, *113*, C04031, doi:10.1029/2007JC004096.

Marshall, J., A. Adcroft, C. Hill, L. Perelman, and C. Heisy (1997), A finite-volume, incompressible Navier Stokes model for studies of the ocean on parallel computers, *J. Geophys. Res.*, *102*(C3), 5753–5766.

Marshall, J., H. Johnson, and J. Goodman (2001), A study of the interaction of the North Atlantic Oscillation with ocean circulation, *J. Clim.*, *14*, 1399–1421.

Menary, M. B., D. L. R. Hodson, J. I. Robson, R. T. Sutton, and R. A. Wood (2015), A mechanism of internal decadal Atlantic Ocean variability in a high-resolution coupled climate model, *J. Clim.*, *28*, 7764–7785.

Msadek, R., and C. Frankignoul (2009), Atlantic multidecadal oceanic variability and its influence on the atmosphere in a climate model, *Clim. Dyn.*, *33*, 45–62, doi:10.1007/s00382-008-0452-0.

Peixoto, J. P., and A. H. Oort (1992), *Physics of Climate*, 520 pp., Am. Inst. of Phys., New York.

Piecuch, C. G., and R. M. Ponte (2012), Importance of circulation change to Atlantic heat storage rates on seasonal and interannual time scales, *J. Clim.*, *25*, 350–362.

Redi, M. H. (1982), Oceanic isopycnal mixing by coordinate rotation, *J. Phys. Oceanogr.*, *12*, 1154–1158.

Reynolds, R. W., N. A. Rayner, T. M. Smith, D. C. Stokes, and W. Wang (2002), An improved in situ and satellite SST analysis for climate, *J. Clim.*, *15*, 1609–1625.

Roberts, C. D., F. K. Garry, and L. C. Jackson (2013), A multimodel study of sea surface temperature and subsurface density fingerprints of the Atlantic meridional overturning circulation, *J. Clim.*, *26*, 9155–9174.

Roberts, C. D., D. Calvert, N. Dunstone, L. Hermanson, M. D. Palmer, and D. Smith (2016), On the drivers and predictability of seasonal-to-interannual variations in regional sea level, *J. Clim.*, *29*, 7565–7585.

Robson, J., D. Hodson, E. Hawkins, and R. Sutton (2014), Atlantic overturning in decline?, *Nat. Geosci.*, *7*, 2–3.

Robson, J., P. Ortega, and R. Sutton (2016), A reversal of climatic trends in the North Atlantic since 2005, *Nat. Geosci.*, *9*, 513–517.

Sarafanov, A., A. Falina, A. Sokov, and A. Demidov (2008), Intense warming and salinification of intermediate waters of southern origin in the eastern subpolar North Atlantic in the 1990s to mid-2000s, *J. Geophys. Res.*, *113*, C12022, doi:10.1029/2008JC004975.

Schlesinger, M. E., and N. Ramankutty (1994), An oscillation in the global climate system of period 65–70 years, *Nature*, *367*, 723–726.

Shaffrey, L., and R. Sutton (2004), The interannual variability of energy transports within and over the Atlantic Ocean in a coupled climate model, *J. Clim.*, *17*, 1433–1448.

Sutton, R. T., and D. L. R. Hodson (2005), Atlantic Ocean forcing of North American and European summer climate, *Science*, *309*, 115–118.

Straneo, F., and P. Heimbach (2013), North Atlantic warming and the retreat of Greenland's outlet glaciers, *Nature*, *504*, 36–43.

Sverdrup, H. U. (1947), Wind-driven currents in a baroclinic ocean; with application to the equatorial currents of the eastern Pacific, *Proc. Natl. Acad. Sci. U. S. A.*, *33*, 318–326.

Theiler, J., S. Eubank, A. Longtin, B. Galdrikian, and J. Doyne Farmer (1992), Testing for nonlinearity in time series: The method of surrogate data, *Physica D*, *58*, 77–94.

Thompson, P. R., C. G. Piecuch, M. A. Merrifield, J. P. McCreary, and E. Firing (2016), Forcing of recent decadal variability in the Equatorial and North Indian Ocean, *J. Geophys. Res. Oceans*, *121*, 6762–6778, doi:10.1002/2016JC012132.

von Storch, H., and F. W. Zwiers (1999), *Statistical Analysis in Climate Research*, 484 pp., Cambridge Univ. Press, Cambridge, U. K.

Watkins, M. M., D. N. Wiese, D.-N. Yuan, C. Boening, and F. W. Landerer (2015), Improved methods for observing Earth's time variable mass distribution with GRACE using spherical cap mascons, *J. Geophys. Res. Solid Earth*, *120*, 2648–2671, doi:10.1002/2014JB011547.

Williams, R. G., V. Roussenov, D. Smith, and M. S. Lozier (2014), Decadal evolution of ocean thermal anomalies in the North Atlantic: The effects of Ekman, overturning, and horizontal transport, *J. Clim.*, *27*, 698–719.

Williams, R. G., V. Roussenov, M. S. Lozier, and D. Smith (2015), Mechanisms of heat content and thermocline change in the subtropical and subpolar North Atlantic, *J. Clim.*, *28*, 9803–9815.

Wunsch, C. (2011), The decadal mean ocean circulation and Sverdrup balance, *J. Mar. Res.*, *69*, 417–434.

Wunsch, C., and P. Heimbach (2007), Practical global oceanic state estimation, *Physica D*, *230*, 197–208.

Wunsch, C., P. Heimbach, R. M. Ponte, and I. Fukumori, and the ECCO-GODAE Consortium Members (2009), The global general circulation of the ocean estimated by the ECCO-Consortium, *Oceanography*, *22*(2), 88–103.

Xu, X., P. B. Rhines, and E. P. Chassignet (2016), Temperature-salinity structure of the North Atlantic circulation and associated heat and freshwater transports, *J. Clim.*, *29*, 7723–7742.

Yeager, S., A. Karspeck, G. Danabasoglu, J. Tribbia, and H. Teng (2012), A decadal prediction case study: Late 20th century North Atlantic Ocean heat content, *J. Clim.*, *25*, 5173–5189.

Yeager, S. G., A. R. Karspeck, and G. Danabasoglu (2015), Predicted slowdown in the rate of Atlantic sea ice loss, *Geophys. Res. Lett.*, *42*, 10,704–10,713, doi:10.1002/2015GL065364.

Zampieri, M., E. Scoccimarro, and S. Gualdi (2013), Atlantic influence on spring snowfall over the Alps in the past 150 years, *Environ. Res. Lett.*, *8*, 034026, doi:10.1088/1748-9326/8/3/034026.

Zhai, X., and L. Sheldon (2012), On the North Atlantic Ocean heat content change between 1955–70 and 1980–95, *J. Clim.*, *25*, 3619–3628.

Zhang, R. (2010), Latitudinal dependence of Atlantic meridional overturning circulation (AMOC) variations, *Geophys. Res. Lett.*, *37*, L16703, doi:10.1029/2010GL044474.

Zhang, R., and T. L. Delworth (2006), Impacts of Atlantic multidecadal oscillations on India/Sahel rainfall and Atlantic hurricanes, *Geophys. Res. Lett.*, *33*, L17712, doi:10.1029/2006GL026267.

Zika, J. D., M. H. England, and W. P. Sijp (2012), The ocean circulation in thermohaline coordinates, *J. Phys. Oceanogr.*, *42*, 708–724.